

This article was downloaded by: [Levitas, Valery]

On: 15 December 2010

Access details: Access Details: [subscription number 931201714]

Publisher Taylor & Francis

Informa Ltd Registered in England and Wales Registered Number: 1072954 Registered office: Mortimer House, 37-41 Mortimer Street, London W1T 3JH, UK



High Pressure Research

Publication details, including instructions for authors and subscription information:

<http://www.informaworld.com/smpp/title~content=t713679167>

Numerical study of stress and plastic strain evolution under compression and shear of a sample in a rotational anvil cell

Valery I. Levitas^{abc}; Oleg M. Zarechnyy^b

^a Department of Mechanical Engineering, Iowa State University, Ames, IA, USA ^b Department of Aerospace Engineering, Iowa State University, Ames, IA, USA ^c Department of Material Science and Engineering, Iowa State University, Ames, IA, USA

Online publication date: 14 December 2010

To cite this Article Levitas, Valery I. and Zarechnyy, Oleg M.(2010) 'Numerical study of stress and plastic strain evolution under compression and shear of a sample in a rotational anvil cell', High Pressure Research, 30: 4, 653 — 669

To link to this Article: DOI: 10.1080/08957959.2010.534990

URL: <http://dx.doi.org/10.1080/08957959.2010.534990>

PLEASE SCROLL DOWN FOR ARTICLE

Full terms and conditions of use: <http://www.informaworld.com/terms-and-conditions-of-access.pdf>

This article may be used for research, teaching and private study purposes. Any substantial or systematic reproduction, re-distribution, re-selling, loan or sub-licensing, systematic supply or distribution in any form to anyone is expressly forbidden.

The publisher does not give any warranty express or implied or make any representation that the contents will be complete or accurate or up to date. The accuracy of any instructions, formulae and drug doses should be independently verified with primary sources. The publisher shall not be liable for any loss, actions, claims, proceedings, demand or costs or damages whatsoever or howsoever caused arising directly or indirectly in connection with or arising out of the use of this material.

Numerical study of stress and plastic strain evolution under compression and shear of a sample in a rotational anvil cell

Valery I. Levitas^{a,b,c*} and Oleg M. Zarechnyy^b

^aDepartment of Mechanical Engineering, Iowa State University, Ames, IA 50011, USA; ^bDepartment of Aerospace Engineering, Iowa State University, Ames, IA 50011, USA; ^cDepartment of Material Science and Engineering, Iowa State University, Ames, IA 50011, USA

(Received 20 September 2010; final version received 18 October 2010)

The large-strain problem on the evolution of distribution of the components of stress tensor and plastic strain in a sample under compression and torsion in a rotational anvil cell was formulated and studied in detail using the FEM. Results are obtained for compression by different axial forces and torsion under two different constant axial forces. The effects of redistribution of the friction radial and torsional stresses and the load on a sample and gasket on the resultant fields are elucidated. Small pressure self-multiplication effect is revealed during torsion after compression below some critical force, and significant heterogeneity of all fields is found. Strong shear strain localization near the contact surface between sample and anvil is quantified. Results are compared with the simplified solution and available experiments. The results obtained are important for the determination of elastic and plastic properties of materials under high pressure and for the interpretation of kinetics of strain-induced phase transformations and chemical reactions.

Keywords: rotational anvil cell; high pressure; finite-element method

1. Introduction

Bridgman anvils and diamond anvils are widely used to produce high pressures and to study material behavior in high-pressure physics, chemistry, material science, geophysics, and technology. High pressures are produced in the process of large elastoplastic deformation of a gasket and, in most cases, of a sample. Unless tested inside hydrostatic media, the stress state of a sample is nonhydrostatic and knowledge of all components of the stress tensor is required [1–5]. In general, a very heterogeneous distribution of all components of stress tensor is present in experiments. Knowledge of the stress tensor combined with X-ray measurements of distances between atomic planes may lead to a more accurate determination of the elastic properties of materials. In rotational Bridgman anvils [6–9] and rotational diamond anvils [10–15], large plastic shear deformation can be superposed on high pressures, due to the rotation of one of the anvils with respect to another (Figure 1(a)). Rotational anvils have been used to study the pressure-dependence of the yield strength in shear [6] and the effect of shear on various phase

*Corresponding author. Email: vlevitas@iastate.edu

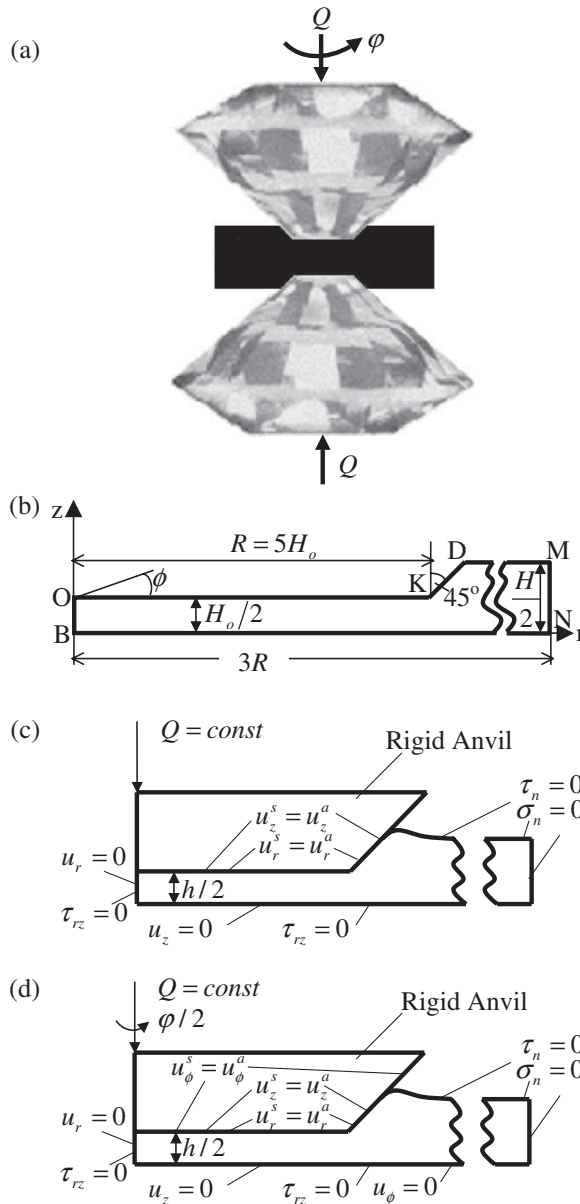


Figure 1. (a) Schematics of rotational diamond anvil cell. (b) Undeformed geometry of a quarter of cross-section of the sample and gasket. (c) Boundary conditions for the problem on compression of sample and gasket by axial force Q . (d) Boundary conditions for the problem on torsion of sample and gasket under constant axial force Q .

transformations and chemical reactions [7–15]. The effect of the plastic shear was found to be very strong and unique. Thus, it leads to: (a) a significant reduction (by a factor of 2–5) in pressure for the initiation of phase transformation and chemical reaction; (b) a significant reduction in pressure hysteresis; (c) the appearance of new phases, which were not obtained without plastic shear; (d) the replacement of a reversible phase transformation by an irreversible one; and (e) athermal strain-controlled kinetics [7–13, 15–17]. To determine the plastic properties and to understand the above-mentioned phenomena and find methods to utilize them, it is necessary to have a

quantitative knowledge of the distribution of the stress tensor in and plastic flow of the deformed material.

Plastic flow and stress distributions can be found numerically using the theory of large plastic deformation. The finite-element method (FEM) was utilized to study distribution of all components of stress tensor and plastic flow under compression in [18–23]. However, a similar problem under compression and shear (torsion) was not treated in the literature. It is much more sophisticated, because it is three-dimensional and because much larger and very localized plastic deformations lead to significant numerical problems. The only existing analytical solution to this problem [16,17] contains a number of simplifying assumptions. In this paper we present our approach and a detailed FEM study of a plastic flow and evolution of distribution of components of stress tensor in a sample under compression and shear in a rotational cell. Results are compared with the simplified solution in [16,17] and with the available experiments.

The paper is organized as follows. In Section 2, a simple generic model for elastoplastic deformations at finite strains is presented. Problem formulation is described in Section 3, and studies of the compression stage and the torsion of a sample under constant axial force are presented in Sections 4 and 5, respectively. Section 6 contains comparisons with available simplified solutions and experiments. In particular, predicted pressure distribution along the radius of a sample and its independence of the anvil rotation are in good correspondence with the experiment. Also, accepted complete-cohesion contact condition reproduces well the direction of contact friction stress and relative sliding along the anvil surface that follow from the model, which allows sliding. This means that large strain localization near the contact surface leads to effective substitution of a cohesion condition with a sliding condition. Section 7 contains concluding remarks. Some preliminary results can be found in our short letter [24].

2. Model for elastoplastic deformations at finite strains

To obtain generic results, we will consider the simplest model for isotropic, perfectly plastic material, which is described, for example, in [25]. More complex models with isotropic and anisotropic hardening are broadly described in the large-strain literature. Justification for the application of the perfectly plastic and isotropic model comes from a postulate about the existence of the limiting surface of the perfect plasticity [25]: it was found for more than 60 materials belonging to different classes (metals, geological materials, oxides, pressed powders, etc.) that above some level of plastic strain and for a monotonous deformation path (*i.e.* without sharp changes in loading directions), the initially isotropic polycrystalline materials are deformed as perfectly plastic and isotropic with a strain-history-independent limiting surface of the perfect plasticity. This means that: (1) the strain hardening is saturated and plastic properties (and the defect structure) reached their steady state; and (2) strain-induced anisotropy does not exhibit itself at monotonous loading. Perfectly plastic behavior starts at the accumulated plastic strain $q > 1$ for metals and for $q > 0.4$ for geological materials.

Let the motion of the deformed body be described by the vector function $\mathbf{r} = \mathbf{r}(\mathbf{r}_0, t)$, where \mathbf{r}_0 and \mathbf{r} are the position vectors in the undeformed configuration and in the deformed configuration at time t . The deformation gradient tensor, $\mathbf{F} = \partial\mathbf{r}/\partial\mathbf{r}_0$, can be multiplicatively decomposed into elastic, \mathbf{F}_e , and plastic, $\bar{\mathbf{F}}_p$, parts, $\mathbf{F} = \mathbf{F}_e \cdot \bar{\mathbf{F}}_p$. It is convenient to decompose $\mathbf{F}_e = \mathbf{V}_e \cdot \mathbf{R}$ into the symmetric elastic stretch tensor \mathbf{V}_e and the orthogonal rigid-body rotation tensor \mathbf{R} . Then, $\mathbf{F} = \mathbf{V}_e \cdot \mathbf{R} \cdot \bar{\mathbf{F}}_p = \mathbf{V}_e \cdot \mathbf{F}_p$, where $\mathbf{F}_p = \mathbf{R} \cdot \bar{\mathbf{F}}_p$ is the rotated plastic deformation gradient tensor. We introduce elastic deformation measures $\mathbf{C}_e = \mathbf{V}_e \cdot \mathbf{V}_e$ and $\mathbf{B}_e = 0.5(\mathbf{C}_e - \mathbf{I})$ and plastic deformation rate $\mathbf{d}_p = (\dot{\bar{\mathbf{F}}}_p \cdot \bar{\mathbf{F}}_p^{-1})_{\text{sym}}$, where subscript sym means symmetrization of a tensor and \mathbf{I} is the unit second-rank tensor. Then, the total system of equations includes [25] the following.

Decomposition of deformation rate $\mathbf{d} = (\dot{\mathbf{F}} \cdot \mathbf{F}^{-1})_{\text{sym}}$ into elastic and plastic parts:

$$\mathbf{d} = \overset{\nabla}{\mathbf{B}}_e - 2(\mathbf{d} \cdot \mathbf{B}_e)_{\text{sym}} + \mathbf{C}_e \cdot \mathbf{d}_p; \quad (1)$$

Elasticity law:

$$\mathbf{T} = \rho \mathbf{V}_e \cdot \frac{\partial \psi}{\partial \mathbf{B}_e} \cdot \mathbf{V}_e; \quad (2)$$

Yield condition and plastic flow rule:

$$Y(\mathbf{T}) \leq 0; \quad \mathbf{d}_p = \mathbf{f}(\mathbf{T}); \quad (3)$$

Mechanical equilibrium equation:

$$\nabla \cdot \mathbf{T} = 0. \quad (4)$$

Here, $\overset{\nabla}{\mathbf{B}}_e = \dot{\mathbf{B}}_e + 2(\mathbf{B}_e \cdot \mathbf{W})_{\text{sym}}$ is the objective (*i.e.* independent of rigid-body rotation) Jaumann time derivative, $\mathbf{W} = (\dot{\mathbf{F}} \cdot \mathbf{F}^{-1})_a$ is the skew-symmetric spin tensor, subscript a denotes the skew-symmetric part of a tensor, ρ is the mass density in the deformed state, ψ is the elastic potential, \mathbf{T} is the true Cauchy stress tensor, and ∇ is the nabla operator in the deformed configuration.

We will focus on the case in which elastic strains are small, but plastic strain and rotation are finite. Representing $\mathbf{V}_e = \mathbf{I} + \boldsymbol{\varepsilon}_e$ with small elastic strain $\boldsymbol{\varepsilon}_e \ll \mathbf{I}$, we present the simplest version of Equations (1)–(3), as follows.

Decomposition of deformation rate into elastic and plastic contributions:

$$\mathbf{d} = \overset{\nabla}{\boldsymbol{\varepsilon}}_e + \mathbf{d}_p; \quad (5)$$

Hooke's elasticity law:

$$p = K \varepsilon_{e0}; \quad \mathbf{s} = 2G \text{dev} \boldsymbol{\varepsilon}_e; \quad (6)$$

Von Mises yield condition and the associated plastic flow rule: in the elastic region,

$$\sigma_i < \sigma_y; \quad \mathbf{d}_p = 0; \quad (7)$$

in the plastic region,

$$\sigma_i = \sigma_y; \quad \mathbf{d}_p = \lambda \mathbf{s}; \quad \lambda = \frac{3 \mathbf{s} \cdot \mathbf{d}}{2 \sigma_y^2}. \quad (8)$$

Here, K is the bulk modulus, G the shear modulus, p the mean pressure, dev the deviatoric operator, ε_{e0} the volumetric elastic strain, $\sigma_i = (3/2 \mathbf{s} \cdot \mathbf{s})^{1/2}$ the stress intensity, $\mathbf{s} = \text{dev} \mathbf{T}$ the deviatoric part of the Cauchy stress, and σ_y the yield strength in compression.

Accumulated plastic strain (Odqvist parameter) is defined by equation $\dot{q} = (2/3 \mathbf{d}_p : \mathbf{d}_p)^{1/2}$. Equation (8)₃ for the scalar λ is derived in the following way. Differentiating the deviatoric part of Hooke's law Equation (6)₂ $\overset{\nabla}{\mathbf{s}} = 2G \overset{\nabla}{\text{dev}} \boldsymbol{\varepsilon}_e$ and expressing $\overset{\nabla}{\text{dev}} \boldsymbol{\varepsilon}_e$ from deviatoric part of Equation (5) and using the flow rule Equation (8)₂, we obtain $\overset{\nabla}{\mathbf{s}} = 2G (\text{dev} \mathbf{d} - \mathbf{d}_p) = 2G (\text{dev} \mathbf{d} - \lambda \mathbf{s})$. Then substituting the derived relationship in the time derivative of the squared yield condition Equation (8)₁, $(3/2) \mathbf{s} : \overset{\nabla}{\mathbf{s}} = 0$, we obtain an equation for the scalar λ , which can be resolved in the form of Equation (8)₃.

Smallness of volumetric elastic strain $\varepsilon_{0e} = p/K < 0.1$ limits the maximum pressure $p < 0.1 K$. Then, we can neglect the elastic deformations of the diamond anvils or anvils made of

hard alloys. Smallness of elastic deviatoric strains is not a limiting assumption because deviatoric stress is limited by the yield strength. We will use material data typical of strengthened steel: $K = 175$ GPa, Poisson's ratio $\mu = 0.2525$, and $\sigma_y = 1.6$ GPa. Consequently, $G = 3K(1 - 2\mu)/(2 + 2\mu) = 104$ GPa, the yield strength in shear $\tau_y = \sigma_y/\sqrt{3} = 0.92$ GPa (according to von Mises' yield condition), and maximum elastic shear strain is $\tau_y/2G = 0.004 \ll 0.1$.

For solution, all stresses are normalized by the yield strength in compression σ_y , $\bar{\mathbf{T}} = \mathbf{T}/\sigma_y$ (e.g. $\bar{\sigma}_{zz} = \sigma_{zz}/\sigma_y$ and $\bar{p} = p/\sigma_y$) and the only material properties used are the dimensionless bulk modulus $\bar{K} = K/\sigma_y = 109.4$ and Poisson's ratio $\mu = 0.2525$. For the convenience of the presentation of results, dimensionless shear stresses, $\bar{\tau}_{rz} = \tau_{rz}/\tau_y$ and $\bar{\tau}_{r\phi} = \tau_{r\phi}/\tau_y$, will be normalized by the yield strength in shear τ_y . Dimensionless, averaged axial stress is defined as $F = Q/(S\sigma_y)$, where Q is the axial force and S is the initial contact area between the sample with a gasket and an anvil.

3. Problem formulation

Figure 1(a) and (b) represents the schematics of rotational diamond anvil cell as well as the geometry of the sample and gasket before application of an axial load. Since the anvil contains 16, 24, or 32 facets, it can be approximated by cone, and the axisymmetric geometry approximation can be used without a significant error. The cylindrical coordinate system $r\phi z$ is used. While we will consider homogeneous material, part of the material below the flat anvil surface (*i.e.* for $r \leq R$, where R is the anvil radius) will be called "sample" and the material at $r > R$ will be called "gasket". Sample and gasket are pre-indented to create the geometry shown in Figure 1(b). Due to symmetry about rotation axis and with respect to the plane passing through the center of a sample, a quarter of a cross section is shown. The following parameters for the initial sample and gasket geometry are chosen: initial thickness of the pre-indented part of a sample between flat diamond surfaces, $H_0 = 0.2 R = 0.5 H$, where H is the thickness of the gasket; the external radius of the gasket is chosen as $3R$.

Two loading regimes are considered: first, the sample is compressed by the increasing axial force Q , and then the torsion of an anvil by an angle φ is applied under constant axial load Q . As initial conditions, all stresses and strains are assumed to be zero. The following boundary conditions are applied for both regimes (Figure 1(c) and 1(d)).

At the axis of rotation OB ($r = 0$), we have shear stress $\tau_{rz} = 0$ and radial displacement $u_r = 0$. At the plane of symmetry $z = 0$, we have shear stress $\tau_{rz} = 0$ and axial displacement $u_z = 0$. At the contact surface between sample, gasket, and rigid anvil OKD, all displacements of the sample are equal to the displacement of the anvil, *i.e.* complete cohesion between anvil and sample is assumed. Normal σ_n and shear τ_n components of the surface traction vector at the deformed free surfaces DM and MN are zero, $\sigma_n = \tau_n = 0$. In addition to the above boundary condition, the following regime-specific boundary conditions are applied.

For the compression stage, the increasing vertical force Q is applied to the rigid anvil, which moves down in the vertical direction. Alternatively, vertical displacement of an anvil can be prescribed. Due to complete cohesion, radial displacement $u_r = 0$ at the contact surface. Due to axial symmetry, twisting shear stress $\tau_{r\phi} = 0$ everywhere.

For the torsion stage, the force Q (and consequently, the averaged axial stress F) is kept constant, and rotation of one anvil with respect to another by growing angle φ is applied. For torsion, the geometry and all fields are axisymmetric, but loading is three-dimensional. Due to symmetry with respect to plane $z = 0$, the twisting displacements $u_\phi = 0$ can be prescribed at this plane, and the half of the rotation angle $\varphi/2$ is applied to the anvil and (due to cohesion) to the contact surface of the sample OKD.

Let us discuss the condition of complete cohesion at the anvil sample and gasket surface. When pressure exceeds $2\sigma_y$, asperities of the diamond or a hard alloy penetrate into a deformed sample, which leads to complete cohesion. However, when the magnitude of the shear friction stress, τ , along the anvil sample and gasket surface, $\tau = \sqrt{\tau_{rz}^2 + \tau_{r\phi}^2}$, reaches the yield stress in shear, the sliding is localized within a thin layer of a sample material in the form of the shear band, just below the contact surface. Since theory does not possess any intrinsic length scale, the width of the shear band tends to zero. This is equivalent to the sliding condition just below the contact surface:

$$\frac{\mathbf{v}}{|\mathbf{v}|} = \frac{\boldsymbol{\tau}}{\tau} \quad \text{for } \tau = \tau_y; \quad \mathbf{v} = 0 \quad \text{for } \tau < \tau_y, \quad (9)$$

where \mathbf{v} is the vector of the particle-relative sliding with respect to the contact surface and near the contact surface. The collinearity of the the directions of sliding and shear friction stresses in Equation (9) is a consequence of isotropy of the plasticity condition. Equation (9) is the isotropic version of a more general contact friction rule for an anisotropic yield condition [25]. Note that for an axisymmetric (or plane) problem the slip-line method results in the same relationship between cohesion at the contact surface and sliding just below it [25].

The FEM software ABAQUS [26] is used for solution of the above-formulated problem. In order to obtain a reliable solution, the problem was solved in number of steps. After each loading step, the ABAQUS built-in mesh-to-mesh solution-mapping procedure was performed. Mapping a solution from one mesh to another is a part of a remeshing procedure, in which a significantly deformed mesh is replaced with a new one. After generating a new mesh, a solution from the previous step is mapped onto the new mesh and analysis continues with the solution from the previous step assumed as the initial condition for the next step. Then, further loading is applied until again the mesh becomes significantly deformed. During all steps, the mesh of the sample has on average 6000–7000 linear quadrilateral elements.

In the FEM, in the contact region where the magnitude of the shear friction stress τ approaches τ_y , a shear band is localized in the first layer of finite elements near the contact surface, imitating the sliding. To receive almost a mesh-independent solution, the size of the first finite-element layer should be much smaller than the sample height h . One can also utilize models of hardening material or viscoplastic material, which would not possess mesh-dependence similar to a perfectly plastic model. However, it complicates the calculations without a significant advantage in accuracy. As we will see below, with a complete-cohesion boundary condition, we can well reproduce an inclination of the vectors \mathbf{v} and $\boldsymbol{\tau}$ relative to the radial direction obtained analytically with the relative sliding condition in [16,17].

4. Analysis of the compression stage

Distribution of pressure and some components of the stress tensor are presented in Figures 2 and 3. During the initial stage of compression, stress evolution is completely controlled by the development of friction shear stresses at the contact surface between the anvil and the sample with gasket. Intense growth of shear stress starts at the external radius of the sample and decays toward the sample's center. This leads to the growth in normal stresses and pressure proportional to the local friction stress and constant normal stresses and pressure in the region where friction stress is still zero. Normal stresses also grow due to the increase in the pressure at the edge of an anvil $r = R$ due to similar (but less intense due to larger thickness) processes in the gasket. With an increase in the applied load or displacement, shear friction stress grows and the region with nonzero shear stress expands, which intensifies the increase in normal stresses and pressure. Growth of the local shear stress stops when it reaches the yield stress in shear; in this region, intense sliding occurs

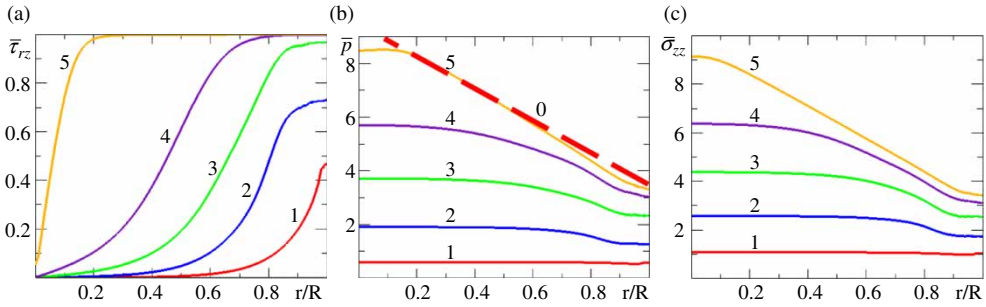


Figure 2. Distribution of (a) dimensionless shear stress $\bar{\tau}_{rz}$, (b) pressure \bar{p} , and (c) normal stress $\bar{\sigma}_{zz}$ along the radius of the contact surface of a sample r for the different values of averaged dimensionless axial stress: (1) $F = 0.95$; (2) $F = 1.91$; (3) $F = 2.86$; (4) $F = 3.68$; (5) $F = 4.29$.

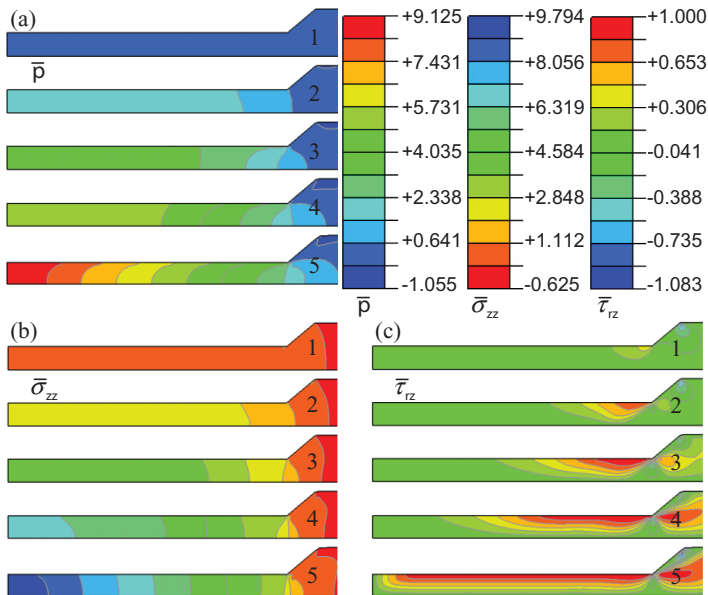


Figure 3. Distribution of (a) dimensionless pressure \bar{p} , (b) normal stress $\bar{\sigma}_{zz}$, and (c) shear stress $\bar{\tau}_{rz}$ for different values of the averaged dimensionless axial stress F in a quarter of cross-section of the sample: (1) $F = 0.95$; (2) $F = 1.91$; (3) $F = 2.86$; (4) $F = 3.68$; (5) $F = 4.29$.

just below the contact surface. A reducing region with almost homogeneous normal stresses exists until nonzero friction stress approaches the center of the sample. During further compression, the region where friction stress reached the yield strength in shear propagates toward the center of the sample. In the region with maximum friction stress, normal stresses and pressure grow linearly, with the exception of the small portion of a sample near the edge $r = R$, where normal stresses are almost constant.

Contour lines in Figure 3 allow us to understand evolution of stresses in the entire cross section of the sample. The region with increased shear stress expands from the edge toward both the center and the symmetry plane of the sample. At some stage, the region appears where shear stress is practically independent of radius and varies almost linearly from zero at the symmetry plane to the yield strength in shear at the contact surface. Normal stress σ_{zz} is practically independent of the z coordinate in most of the sample, while pressure reduces from the contact surface to the plane of symmetry.

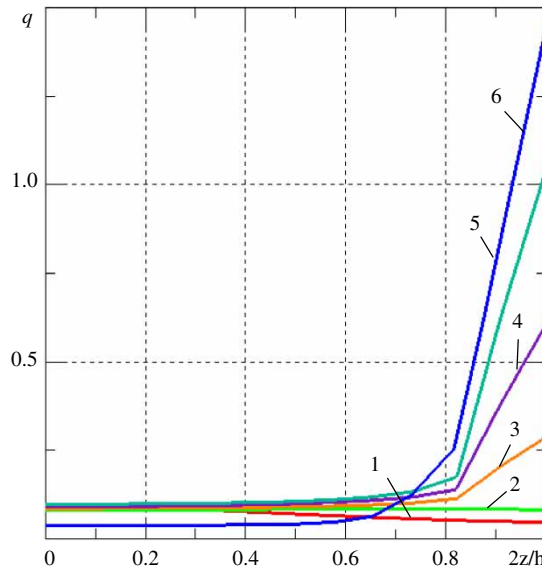


Figure 4. Distributions of the accumulated plastic strain q (Odqvist parameter) along the dimensionless width of the sample $2z/h$ for sections with different values of dimensionless radius r/R after compression with averaged dimensionless axial stress $F = 4.29$: (1) $r/R = 0$; (2) $r/R = 0.2$; (3) $r/R = 0.4$; (4) $r/R = 0.6$; (5) $r/R = 0.8$; (6) $r/R = 1.0$

It is not representative to show the contour lines for the Odqvist parameter due to strong concentration of plastic strain near the contact surface. That is why distributions of the accumulated plastic strain q along the z coordinate for six sections with different distances r/R from the center are shown in Figure 4 after compression by the averaged axial stress $F = 4.29$. Note that the thickness of the sample did not change much and that for homogeneous uniaxial compression $q = \ln(H_o/h) = 0.05$ for $F = 3.68$ and $q = \ln(H_o/h) = 0.10$ for $F = 4.29$. These values correspond to the Odqvist parameter in the vicinity of the plane of symmetry of the sample, where plastic shears are absent. Shear strain localization near contact increases the Odqvist parameter significantly, up to $q = 1$ and higher, with larger values for larger r . This means that even during the compression stage, large plastic strains are concentrated near the contact surface due to contact friction, and material is under compression and shear, similar to the case with the rotation of an anvil. In the lower part of the sample $2z/h < 0.6$, accumulated plastic strain is relatively homogeneous along both r and z and changes with compression approximately like $\ln(H_o/h)$. Knowledge of the evolution of accumulated plastic strain is important for the simulation of strain-induced phase transformation [27]. Namely, the larger the plastic strain in the region where pressure exceeds some critical value, the greater the phase transformation progress is.

5. Analysis of the torsion of a sample under constant axial force

Torsion was performed under two different values of axial force: for the case with averaged axial stress $F = 4.29$, for which friction shear stress reached the shear strength almost along the entire contact surface (excluding the central part of the sample; see curve 5 in Figure 2), and for the case with $F = 3.68$, for which friction stress reaches the shear strength along the external half of the radius only (curve 4 in Figure 2). In Figure 5, distributions of dimensionless radial $\bar{\tau}_{rz}$ and torsional $\bar{\tau}_{r\phi}$ shear stresses, as well as pressure \bar{p} along the radius of the contact surface of a sample r , are shown for the averaged dimensionless axial stress $F = 4.29$ and different values

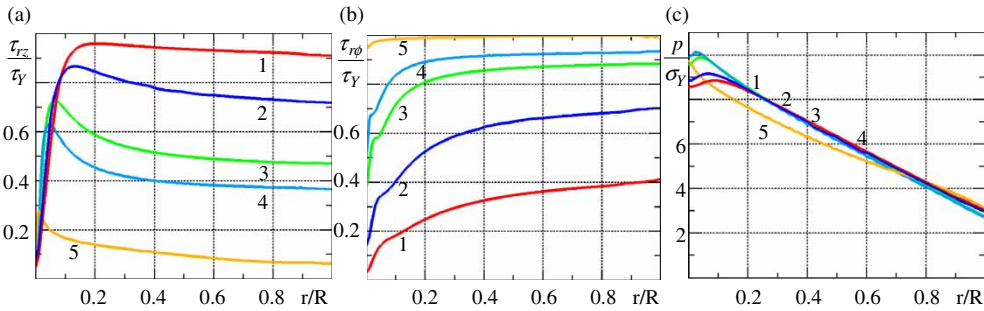


Figure 5. Distribution of (a) dimensionless shear stress $\bar{\tau}_{rz}$, (b) shear stress $\bar{\tau}_{r\phi}$ and (c) pressure \bar{p} along the radius of the contact surface of a sample r for the averaged dimensionless axial stress $F = 4.29$ and different values of angle of rotation φ . (1) $\varphi = 0.03$; (2) $\varphi = 0.21$; (3) $\varphi = 0.958$; (4) $\varphi = 0.1.45$; (5) $\varphi = 2.034$.

of the angle of rotation φ . During torsion, torsional shear stress $\tau_{r\phi}$ increases, is becoming less dependent up on radius, and almost reaches the yield stress in shear τ_y , along almost the entire contact surface of a sample. Radial shear stress τ_{rz} reduces in the region where it reached τ_y during compression because the magnitude of friction shear stress vector $\tau = \sqrt{\tau_{r\phi}^2 + \tau_{rz}^2}$ is equal to the yield strength in shear τ_y . Near the symmetry axis, radial shear stress τ_{rz} increases initially during the rotation of an anvil, because torsion produces sliding in this region and τ is still lower than τ_y . Pressure distribution practically does not change during the rotation of an anvil in most of the sample. Only near the symmetry axis, where shear stresses grow, does pressure slightly grow as well. For large rotation, however, pressure slightly decreases in the central part of a sample because of the pressure growth in the gasket region $r \geq R$, since the total axial force does not change.

The same distributions in the sample volume, as well as the distribution of normal axial stress σ_{zz} are shown in Figure 6. Drastic reduction in the sample thickness during rotation is clearly visible. Radial shear stress τ_{zr} is practically independent of r and varies approximately linearly along the z coordinate (from zero at the symmetry plane to the maximum value at the contact surface), except in the small central region. Torsional shear stress $\tau_{r\phi}$ is weakly dependent on the z coordinate and is becoming almost constant in the entire sample for large rotations. Axial stress σ_{zz} remains almost independent of the z coordinate (like at compression). Pressure p increases from the plane of symmetry to the contact surface (like at compression); however, for large rotation, it is practically the same at the plane of symmetry and the contact surface, with only a small reduction between them. All normal stresses and pressure grow linearly with decreasing r , except near the symmetry axis.

The same distributions and fields as in Figures 5 and 6 are presented in Figures 7 and 8 but for smaller averaged axial stress $F = 3.68$, when after compression, the shear stress τ_{rz} reached the yield strength in shear along the external half of the sample only (Figure 2). At the initial stage of rotation, radial shear stress τ_{rz} increases in the central part of a sample. When the magnitude of the friction stress vector τ reaches the yield strength in shear τ_y , radial shear stress reduces because of the increase in the twisting shear stress $\tau_{r\phi}$. Variation in both shear stresses with rotation is then similar to that for larger averaged axial stress $F = 4.29$ (compare Figures 5 and 7). However, for smaller F , twisting shear stress is slightly smaller (and radial shear stress is slightly larger), for the same rotation angle.

While it was expected that the pressure gradient in the sample will initially grow with rotation because of growth in radial shear stress, pressure gradient and pressure in the most part of a sample slightly reduce. The main reason can be found by analyzing the ratio F_s/F of the axial load F_s applied to the sample (horizontal contact surface of the sample OK) to the total axial load

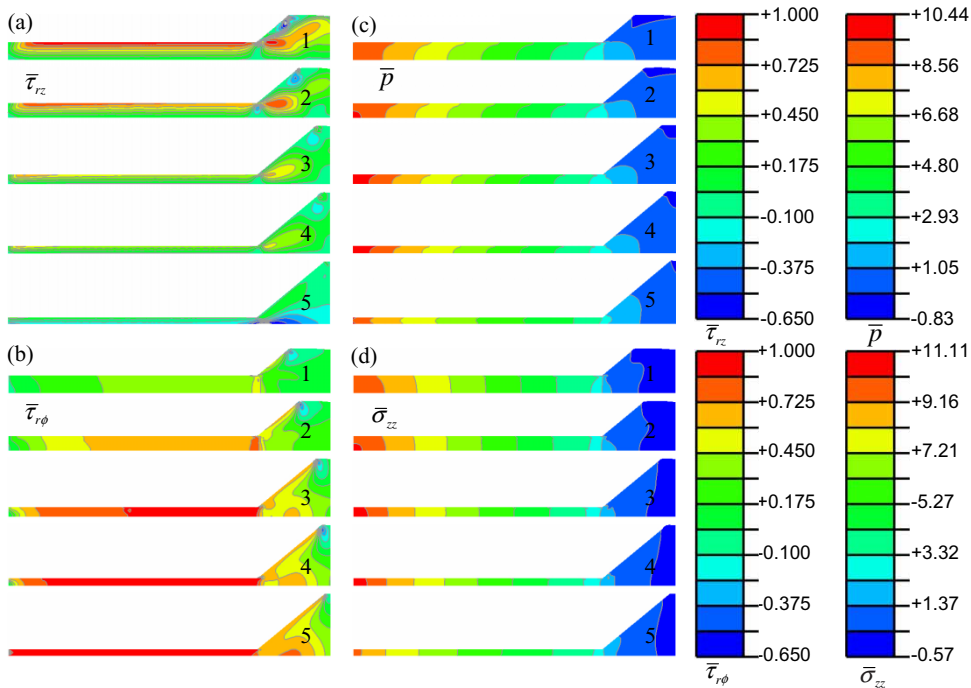


Figure 6. Distribution of (a) dimensionless shear stress $\bar{\tau}_{rz}$, (b) shear stress $\bar{\tau}_{r\phi}$, (c) pressure \bar{p} , and (d) normal stress $\bar{\sigma}_{zz}$ for the averaged dimensionless axial stress $F = 4.29$ and different values of angle of rotation φ in a quarter of a cross-section of the sample. (1) $\varphi = 0.03$; (2) $\varphi = 0.21$; (3) $\varphi = 0.958$; (4) $\varphi = 0.1.45$; (5) $\varphi = 2.034$.

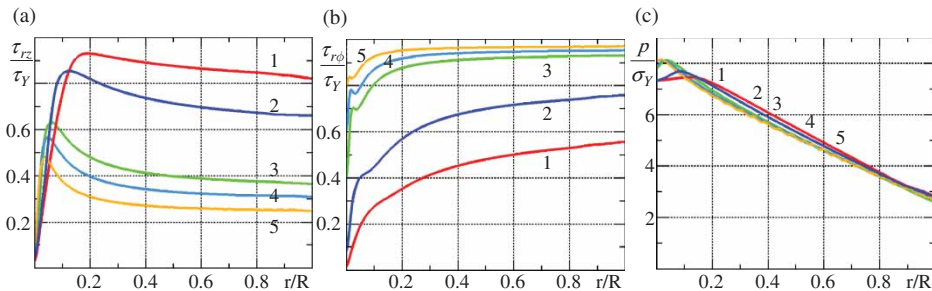


Figure 7. Distribution of (a) dimensionless shear stress $\bar{\tau}_{rz}$, (b) shear stress $\bar{\tau}_{r\phi}$ and (c) pressure p along the radius of the contact surface of a sample r for the averaged dimensionless axial stress $F = 3.68$ and different values of angle of rotation φ . (1) $\varphi = 0.03$; (2) $\varphi = 0.21$; (3) $\varphi = 0.958$; (4) $\varphi = 0.1.45$; (5) $\varphi = 2.034$.

F applied to the sample and gasket, namely, its variation versus angle of rotation of the anvil φ (Figure 9).

At the beginning of torsion under $F = 4.29$, 95% of the axial force is applied to the sample. After rotation by angle $\varphi = 2.368$, the inclined part of the contact surface of a gasket increased by almost 300%, causing the reduction in the ratio F_s/F to 0.89. A sharp decrease in the ratio F_s/F occurs during the initial stage of torsion, $\varphi = 0.04$. For the smaller applied stress F , F_s/F dropped to less than 0.80 during the initial stage of torsion and then changed almost in the same way as in the first case, namely decreased by another 5–6%. That is why the pressure gradient and pressure in the sample slightly reduce during the torsion for $F = 3.68$. Still, the pressure at

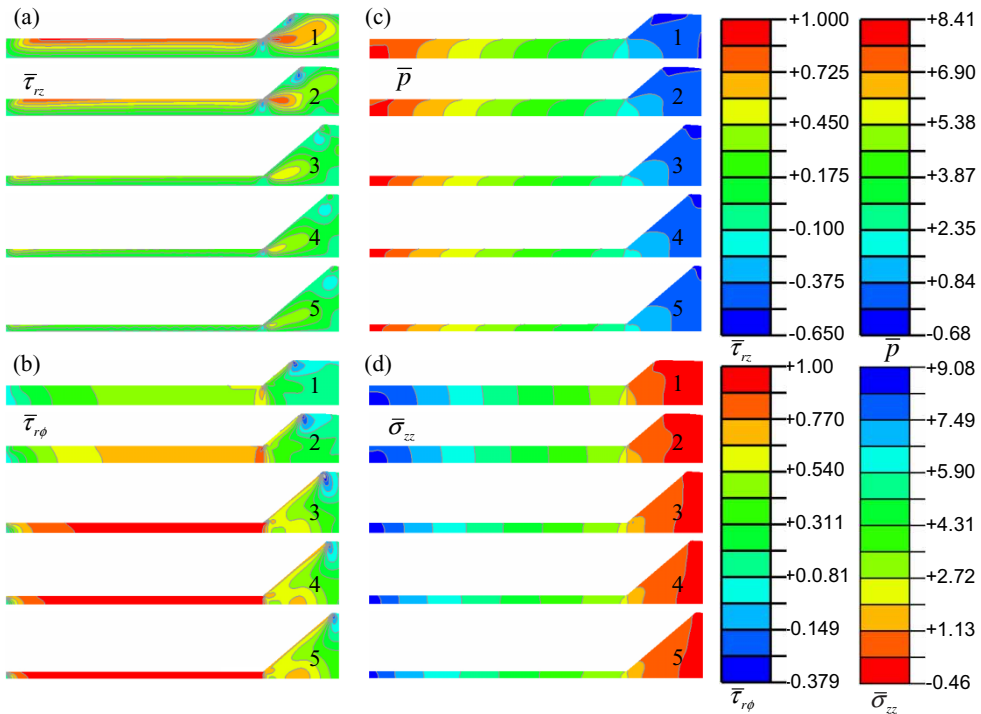


Figure 8. Distribution of (a) dimensionless shear stress $\bar{\tau}_{rz}$, (b) shear stress $\bar{\tau}_{r\phi}$, (c) pressure \bar{p} , and (d) normal stress $\bar{\sigma}_{zz}$ for the averaged dimensionless axial stress $F = 3.68$ and different values of angle of rotation ϕ in a quarter of a cross-section of the sample. (1) $\phi = 0.03$; (2) $\phi = 0.21$; (3) $\phi = 0.958$; (4) $\phi = 0.1.45$; (5) $\phi = 2.034$.

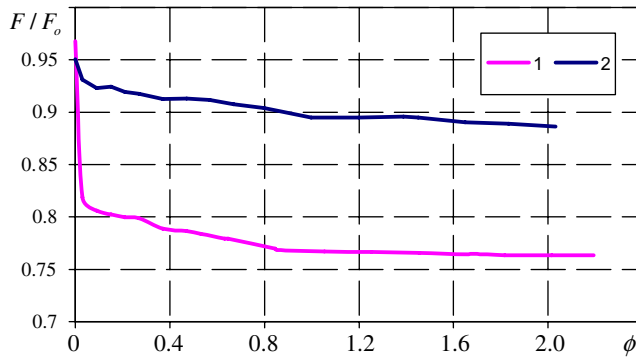


Figure 9. The ratio F_s/F of the axial load F_s applied to the sample (horizontal contact surface of the sample OK) to the total axial load F applied to the sample and gasket versus angle of rotation of the anvil ϕ . (1) $F = 3.68$; (2) $F = 4.29$.

the center of a sample slightly increases. For large anvil rotation, the ratio F_s/F tends toward a plateau that depends on applied force and the geometry of the gasket.

Note that the experimentally observed increase in pressure under constant axial force during rotation of an anvil and phase transformation [10–13] (the pressure self-multiplication effect) was explained in [16,17,28,29] by an increase in the yield strength during the phase transformation. Our current results without phase transformations suggest an additional possible reason for the pressure self-multiplication effect related to an increase in the radial shear stress and pressure redistribution between sample and gasket.

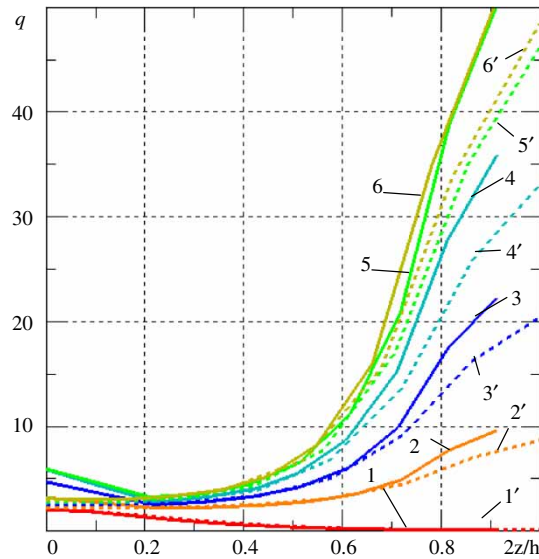


Figure 10. Distributions of the accumulated plastic strain q (Odqvist parameter) along the dimensionless width of the sample $2z/h$ for sections with different values of dimensionless radius r/R compression and torsion by angle $\varphi = 2.034$: (1) $r/R = 0$, (2) $r/R = 0.2$, (3) $r/R = 0.4$, (4) $r/R = 0.6$, (5) $r/R = 0.8$, (6) $r/R = 1.0$. Solid lines correspond to averaged dimensionless axial stress $F = 4.29$ and dashed lines correspond to $F = 3.68$.

The distributions of the components of the stress tensor fields and pressure field in the sample volume (Figure 8) for the axial force $F = 3.68$ is qualitatively similar to the case for $F = 4.29$. Thus, axial stress σ_{zz} is practically independent of the z coordinate and torsional shear stress $\tau_{r\phi}$ is weakly dependent on the z coordinate, and is becoming almost constant in the entire sample for large rotations. Radial shear stress τ_{zr} is practically independent of r . Pressure p increases from the plane of symmetry to the contact surface; however, equality of the pressure at the plane of symmetry and the contact surface (observed for $F = 4.29$ for large rotation) was not obtained for $F = 3.68$.

Figure 10 presents the distributions of the accumulated plastic strain q along the z coordinate for six sections with different r/R values after compression and torsion by an angle $\varphi = 2.04$, for both averaged axial stresses $F = 4.29$ and $F = 3.68$. It is clear that the Odqvist parameter q increases more than by an order of magnitude in comparison with compression without rotation. For the strain-induced phase transformations, the concentration of the high-pressure phase is proportional to the plastic strain [16,17]. Since pressure does not change drastically during rotation and plastic strain growth, this explains the promotion of phase transformations by rotation of an anvil [27].

Plastic strain is larger for rotation under larger axial force. It increases significantly with the increasing radius of the particles r , and it becomes practically independent of r in the ring $0.8 < r/R < 1$. Variation of q along the height is more complex. At symmetry axis $r = 0$, the Odqvist parameter reduces from the plane of symmetry toward zero at the contact surface. This corresponds to the presence of the “rigid” zone near the contact surface and the symmetry axis. For $0.2 < r/R < 1$, maximum accumulated plastic strain is localized at the contact surface with the large gradient; the minimum of q is in the range $0.2 < 2z/h < 0.4$. An important contribution to the accumulated plastic strain during torsion (in addition to shear straining) is related to the reduction in the dimensionless thickness of a sample h/h_0 shown in Figure 11, where h_0 is the sample thickness at the beginning of rotation. The reduction in thickness is caused by the reduction in radial shear friction stress τ_{rz} (due to an increase in $\tau_{r\phi}$), which resists to the radial material flow. The rate of the thickness reduction with respect to an anvil rotation decreases with the rotation angle and is

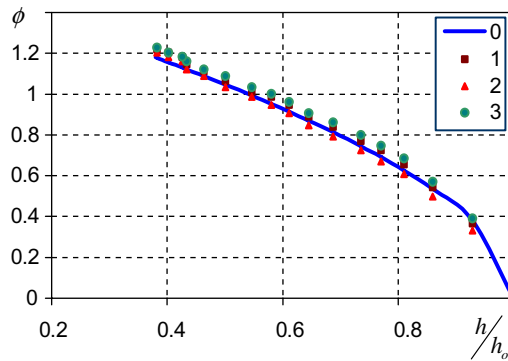


Figure 11. Reduction in the relative thickness of a sample versus the rotation angle of an anvil under constant averaged dimensionless axial stresses $F = 4.29$ (1) and $F = 3.68$ (2) and according to Equation (12) [16].

almost saturated for large angles. Rotation of an anvil under smaller force causes smaller reduction in the sample thickness. When one considers phase transformations that are accompanied by the reduction in volume, thickness reduction compensates for the decrease in volume and increases pressure in the transforming region [16,17]. The rotation-induced reduction in sample thickness was considered in [28,29] as the main macroscopic mechanism for the intensification of phase transformation, before strain-induced kinetics has been introduced [16,17,27].

6. Comparison with simplified solutions

For axisymmetric compression, a simple and much faster solution for stresses using the slip-line method was found in [25]. After adding to two equilibrium equations and to the yield condition, the so-called condition of complete plasticity about the equality of hoop stress and the smaller-magnitude other principal stress, one obtains a system of four equations with four unknown components of the stress tensor. This statically determinate system can be easily solved for each prescribed geometry with the slip-line method (method of characteristics) without considering the kinematics of the flow. While the velocity field for a rigid-plastic model can be determined with the slip-line method, and deformation can be obtained by integrating this field, it was not done in [25]. The case when the friction stress reaches the yield strength in shear on the entire contact surface (excluding a small part near the sample center, obtained from the solution) was treated in [25]. Also, a pressure-dependent yield condition was used in [25].

Despite these differences, there are some common general features between the solution in [25] and here for the case when the friction shear stress reaches the yield strength in shear on almost the entire contact surface (line 5 and contour plot 5 in Figures 2 and 3). Thus, the character of the distribution of all stresses in the sample and at the contact surface is very similar. Stress σ_{zz} is practically independent of the z coordinate, and the contour lines for other normal stresses and pressure look similar for both solutions. If the yield strength in shear in [25] would be pressure-independent, shear stresses would be independent of the r coordinate and would vary linearly along z , as in the current solution. Normal stresses would grow linearly toward the center with the exception of the small portion of a sample near the edge $r = R$, where normal stresses are almost constant, and near the center of a sample, where they grow parabolically (in both the FEM and slip-line solutions).

The only existing solution for the case of torsion under constant axial force is a simplified analytical solution in [16,17]. It considers a cylindrical sample only, *i.e.* the gasket ($r > R$), and

consequently, redistribution of the force and moment between sample and gasket is neglected. It is assumed that the magnitude of the shear friction stress τ is equal to the yield strength in shear τ_y along the entire contact surface and that the angle of inclination of the vector of friction stress τ to the radius is the same everywhere. It operates with stresses at the contact surface only. A simplified equilibrium equation is as follows:

$$\frac{dp}{dr} = \frac{2\tau_{rz}}{h}, \quad (10)$$

where τ_{rz} is taken at the contact surface, and Equation (9) is used as well. Equation (10) was reduced in [16,17] to

$$\frac{dp}{dr} = \frac{2\tau_y}{h_0}. \quad (11)$$

Because the sample thickness at the beginning of rotation, $h_0 = \text{const}$, Equation (11) coincides with the equilibrium equation for compression under the same force F . Thus, the analytical solution predicts linear pressure distribution along the radius, which is the same before and during the rotation stage, *i.e.* it is independent of the rotation of an anvil. It is clearly seen from Figure 2(b) that the analytical solution gives practically the same slope as the FEM solution for $F = 4.29$. It is also clear from the FEM solution that the pressure distribution along the radius under fixed axial force is weakly dependent on the rotation of an anvil for both forces $F = 4.29$ (Figure 5(c)) and $F = 3.68$ (Figure 7(c)). Reasonable agreement for the case with $F = 3.68$ (despite the fact that, under compression, shear stress reached the yield strength at the half of the contact surface only) is related to the fact that rotation quickly increases the magnitude of the friction stress to the yield strength almost on the entire contact surface (excluding the small part near the symmetry axis). Deviation of curve 5 in Figure 5(c) for the large rotation is related to the increase in the pressure in the region of the gasket $r \geq R$ and (in order to keep the same averaged axial stress F) consequently to the reduction in pressure in the sample $r < R$.

Combining Equations (24) and (25) from [16], the following equation connecting angle of rotation of an anvil, φ , and thickness reduction during rotation can be obtained as follows:

$$\varphi = \frac{1 + 0.204 m}{0.204 m} \left(\sqrt{\frac{h_0^2}{h^2} - 1} - \arccos \frac{h}{h_0} \right), \quad (12)$$

where $m = R/H_o$ and h_0 is the sample thickness before rotation starts. For our case, $m = 5$. The plot of h/h_0 versus φ is shown in Figure 11, along with the results of FEM simulation for both $F = 4.29$ and $F = 3.68$. Taking into account the difference in problem formulation for analytical and numerical solutions (in particular, neglecting part of the force acting on the conical surface of an anvil), agreement is quite reasonable.

According to Equation (23) from [16], the angle α between the vector of the velocity of relative sliding of the sample particles with respect to the diamond surface v (and according to Equation (9), between the vector of the friction shear stress τ) and the radial direction r is

$$\alpha = \arccos \frac{h}{h_o} \quad (13)$$

and does not change along the radius. This relationship is compared with more precise numerical results in Figure 12, where angle α was obtained from relationship $\tan \alpha = (\tau_{r\phi}/\tau_{rz})$, assuming that the vectors of relative sliding and contact shear stress are parallel (see Equation (9)). While shear stresses at the contact surface are not constant (excluding τ_{rz} for a small rotation and $\tau_{r\phi}$ for a large rotation), for both averaged axial stresses, $F = 4.29$ and $F = 3.68$, angle α does not

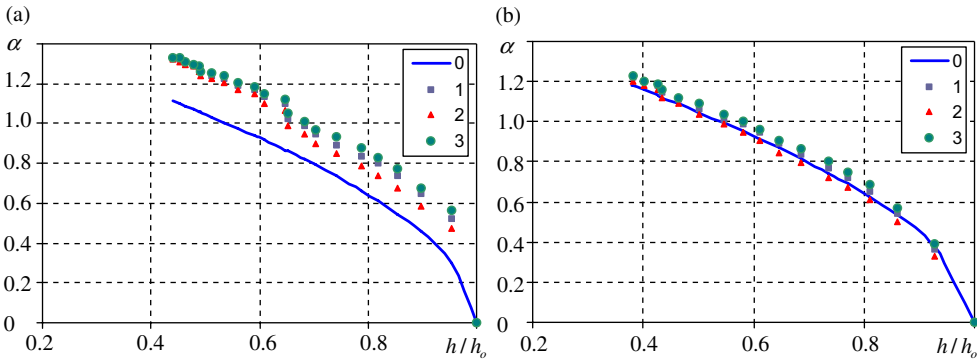


Figure 12. Angle of the velocity of relative sliding of a sample particles with respect to the anvil surface versus reduction of relative thickness of a sample under constant averaged dimensionless axial stress (a) $F = 3.68$ and (b) $F = 4.29$ for $r/R = 0.6$ (1), $r/R = 0.4$ (2), $r/R = 0.8$ (3) and according to Equation (13) [16].

change significantly along the radius. Comparison between the analytical and numerical solutions for $F = 4.29$ is very good. This means both a good quality of a simplified analytical model and the complete adhesion boundary condition (assumed in numerical solution) reproduce well the relative sliding of sample particles just below the contact surface, according to Equation (9). For $F = 3.68$, the numerical solution is above the analytical one; coincidence in this case is not expected because the magnitude of the contact shear stress vector grows during the initial stage of rotation, in contrast to the problem formulation in [16].

Good correspondence between the analytical and FEM solutions in Figures 11 and 12 for the case when friction stress before rotation reaches the yield strength in shear also justifies the relationship between angle of rotation of a sample φ_s (excluding thin near-contact layer) and anvil [16,17]:

$$\varphi_s = \frac{1}{1 + 0.204m} \varphi. \tag{14}$$

The difference $\varphi - \varphi_s$ is due to large localized shear near the contact surface.

For *comparison with experiments*, two points are important. First, that known experimental pressure distributions for compression and compression and torsion [10,13,30] have the same shape as in our simulations (Figures 2, 5, and 7), *i.e.* linear pressure growth toward center in the major part of a sample and parabolic growth near the center of a sample. Second, that the independence of the pressure distribution of the rotation of an anvil was observed *experimentally* for sodium chloride in [10] and for stainless steel in [13], similar to the results of our simulations (Figures 5 and 7). Note that a more detailed comparison is not straightforward because of missing experimental information about sample thickness under load, geometry of gasket, which determines pressure at $r = R$, and the yield strength [25]. However, for the case when all geometric information is known, comparison with the experiment is not very informative (when linear pressure growth is established), because the yield strength is determined by fitting the experimental and theoretical slope of the linear part of the pressure distribution.

7. Concluding remarks

In this paper, the detailed FEM solutions for the evolution of the fields of components of stress tensor and accumulated plastic strain in a sample under compression and torsion in rotational anvils are found. They confirm some of the predictions of a simplified analytical solution [16,17], in some cases quantitatively, namely that (and how) the thickness of a sample significantly reduces during

rotation of an anvil due to reduction in radial friction (which is extremely important for promoting the phase transformations), that normal stress (pressure) distribution along the contact surface during rotation of an anvil is practically independent of rotation (which corresponds to experiments in [10,13]), and that τ_{rz} and $\tau_{r\phi}$ are becoming independent of the r for large enough rotations. Also, the dependence of the direction of the vector of friction stress and velocity of relative sliding at the contact surface versus twisting angle corresponds well to the analytical solution for the case with the axial force $F = 4.29$. However, the FEM solution takes into account much more detail than a simplified model [16,17], such as the variation of all fields in the z -direction, the heterogeneity of shear stresses τ_{rz} and $\tau_{r\phi}$ for moderate anvil rotations, and the effect of the gasket that changes pressure distribution and a portion of the applied force that acts on a sample. FEM allowed us to study compression before shear friction stress reached the yield strength in shear and part of the sample became elastic and the torsion of the sample under these conditions. The FEM solution also revealed a small pressure self-multiplication effect during the rotation of an anvil without phase transformation and significant heterogeneity of accumulated plastic strain, which is important for the determination and interpretation of the kinetics of strain-induced phase transformations and chemical reactions.

One of the methods to determine the pressure dependence of the shear strength [6,31] was based on assumptions that $\tau_{r\phi} = \tau_y$ and pressure are homogeneous along the radius. The $\tau_{r\phi}$ can be determined through the measured torque, and pressure is equal to force divided by area. It is clear that while $\tau_{r\phi}$ can be very close to τ_y for large rotations, it is still smaller, since $\tau_{rz} \neq 0$. Pressure is extremely heterogeneous, and if the yield strength depends on pressure, it will be heterogeneously distributed as well. Stresses on the inclined part of an anvil produce 23% of the measured force, which introduces additional inaccuracy. Also, for small rotations, $\tau_{r\phi}$ and consequently torque grow with increases in ϕ , which can be interpreted as strain hardening, while we consider material without strain hardening. Thus, this method contains significant errors. Alternative methods that do not use the rotation of an anvil and are based on the measurement of pressure distribution (or force) and sample thickness [25] are much more accurate and preferable but work for large strain only, when strain hardening is saturated.

Drastic heterogeneity in accumulated plastic strain, in both the axial and radial directions, as well as strong radial heterogeneity in pressure, causes a significant problem in the quantitative characterization of strain-induced phase transformations and chemical reactions. Current experimental approaches allow one to measure in local points the concentration of a high-pressure phase [14,15,32]. With the Raman method, concentration is averaged over the thin layer near the sample contact surface, where strong plastic strain localization occurs. With X-ray diffraction, the concentration of a high-pressure phase is averaged over the thickness of a sample (or over a major portion of the thickness). Consequently, the results and interpretation of the kinetic data have to be different with different measurement techniques. This indeed was observed experimentally in [32], where phase transformation in Si under compression in diamond anvils was found in a thin contact layer only and not in the bulk. Since stress intensity is constant and pressure does not vary significantly along the thickness but plastic strain does, this difference is a signature of the strain-induced phase transformation. Strong strain localization near the contact surface implies that strain-induced transformations and reactions and new strain-induced phases can be detected in the contact layer using the Raman method. The results obtained on the distribution of components of stress tensor and accumulated plastic strain are an important step in the determination of local kinetic equations for strain-induced phase transformations [27].

Acknowledgement

ARO (W911NF-09-1-0001), DTRA (HDTRA1-09-1-0034), ISU, and TTU support for this research is gratefully acknowledged.

References

- [1] T.S. Duffy, G. Shen, D.L. Heinz, J. Shu, Y.Z. Ma, H.K. Mao, R.J. Hemley, and A.K. Singh, *Lattice strains in gold and rhenium under nonhydrostatic compression to 37 GPa*, Phys. Rev. 60 (1999), pp. 15063–15073.
- [2] W.B. Durham, D.J. Weidner, S.I. Karato, and Y. Wang, *Plastic deformation of minerals and rocks*, in *Reviews in Mineralogy and Geochemistry*, S.I. Karato and H.R. Wenk, eds., Vol. 51, Mineralogical Society of America, Washington, DC, 2002, pp. 21–49.
- [3] H.R. Wenk, S. Matthies, R.J. Hemley, H.K. Mao, and J. Shu, *The plastic deformation of iron at pressures of the Earth's inner core*, Nature 405 (2000), pp. 1044–1047.
- [4] H.P. Liermann, S. Merkel, L. Miyagi, H.R. Wenk, G. Shen, H. Cynn, and W.J. Evans, *Experimental method for in situ determination of material textures at simultaneous high pressure and high temperature by means of radial diffraction in the diamond anvil cell*, Rev. Scient. Instrum. 80 (2009), 104501, pp. 1–8.
- [5] S. Merkel, C.N. Tome, and H.R. Wenk, *Modeling analysis of the influence of plasticity on high pressure deformation of hcp-Co*, Phys. Rev. B 79 (2009), 064110, pp. 1–13.
- [6] P.W. Bridgman, *Studies in Large Plastic Flow and Fracture*, McGraw Hill, New York, 1952.
- [7] P.W. Bridgman, *Effect of high shear stress combined with high hydrostatic pressure*, Phys. Rev. 48 (1935), pp. 825–847.
- [8] N.S. Enikolopian, *Some aspects of chemistry and physics of plastic flow*, Pure Appl. Chem. 57 (1985), pp. 1707–1711.
- [9] A.A. Zharov, *Reaction of solid monomers and polymers under shear deformation and high pressure*, in *High Pressure Chemistry and Physics of Polymers*, A.L. Kovarskii, ed., CRC Press, Boca Raton, Florida, 1994, pp. 267–301.
- [10] V.D. Blank, Y.Y. Boguslavski, M.I. Eremetz, E.S. Izkevich, Y.S. Konyaev, A.M. Shirokov, and E.I. Estrin, *Pressure self-multiplication effect at phase transition under quasi-hydrostatic conditions*, Sov. Phys. JETP 87 (1984), pp. 922–926.
- [11] M.M. Aleksandrova, V. Blank, A. Golobokov, Y.S. Konyaev, and E. Estrin, *Effect of shear straining under the pressure on phase transition semiconductor–metal in indiy telluride*, Solid State Phys. 29 (1987), pp. 2573–2578.
- [12] M.M. Aleksandrova, V. Blank, and S. Buga, *Phase transition in Ge and Si under shear strain under pressure up to 12 GPa and P–T–g diagrams of these elements*, Solid State Phys. 35 (1993), pp. 1308–1317.
- [13] N. Novikov, S. Polotnyak, L. Shvedov, and V.I. Levitas, *Phase transition under compression and shear in diamond anvils: Experiment and theory*, Superhard Mater. 3 (1999), pp. 39–51.
- [14] V.I. Levitas, Y.Z. Ma, and J. Hashemi, *Transformation-induced plasticity and cascading structural changes in hexagonal boron nitride under high pressure and shear*, Appl. Phys. Lett. 86 (2005), 071912, pp. 1–3.
- [15] V.I. Levitas, Y. Ma, J. Hashemi, M. Holtz, and N. Guven, *Strain-induced disorder, phase transformations, and transformation-induced plasticity in hexagonal boron nitride under compression and shear in a rotational diamond anvil cell: In situ x-ray diffraction study and modeling*, J. Chem. Phys. 125 (2006), 044507, pp. 1–14.
- [16] V.I. Levitas, *High-pressure mechanochemistry: conceptual multiscale theory and interpretation of experiments*, Phys. Rev. B 70 (2004), 184118, pp. 1–24.
- [17] V. Levitas, *Continuum mechanical fundamentals of mechanochemistry*, in *High Pressure Surface Science and Engineering*, Y. Gogotsi and V. Domnich, eds., Institute of Physics, Bristol, 2004, pp. 159–292.
- [18] W. Moss and K.A. Goettel, *Finite-element design of diamond anvils*, Appl. Phys. Lett. 50 (1987), pp. 25–27.
- [19] W.C. Moss, J.O. Hallquist, R. Reichlin, K.A. Goettel, and S. Martin, *Finite-element analysis of the diamond anvil cell – achieving 4.6 Mbar*, Appl. Phys. Lett. 48 (1986), pp. 1258–1260.
- [20] S. Weir, J. Akella, C. Ruddle, T. Goodwin, and L. Hsiung, *Static strengths of Ta and U under ultrahigh pressures*, Phys. Rev. B 58 (1998), pp. 11258–11265.
- [21] S. Merkel, R.J. Hemley, and H.K. Mao, *Finite-element modeling of diamond deformation at multimegabar pressures*, Appl. Phys. Lett. 74 (1999), pp. 656–658.
- [22] V.I. Levitas, S.B. Polotnyak, and A.V. Idesman, *Large elastoplastic deformations and stress state of deformable gasket of high pressure apparatus with diamond anvils*, Strength Mater. 221 (1996), pp. 221–227.
- [23] N.V. Novikov, V.I. Levitas, and A.V. Idesman, *Theoretical description of thermomechanical effects in high pressure apparatus*, High Press. Res. 5 (1990), pp. 868–870.
- [24] V.I. Levitas and O.M. Zarechnyy, *Plastic flow under compression and shear in rotational diamond anvil cell: Finite-element study*, Appl. Phys. Lett. 91 (2007), 141919, pp. 1–3.
- [25] V.I. Levitas, *Large Deformation of Materials with Complex Rheological Properties at Normal and High Pressure*, Nova Science Publishers, New York, 1996.
- [26] D. Hibbit, I. Karlsson, and J. Sorenson, *ABAQUS, Version 6.7*, Hibbit, Karlsson and Sorenson Inc., Providence, RI, USA, 2007.
- [27] V.I. Levitas and O.M. Zarechnyy, *Modeling and simulation of mechanochemical processes in rotational diamond anvil cell*, Europhysics Letters 88 (2009), 16004, pp. 1–6.
- [28] V.I. Levitas, *Phase transitions in elastoplastic materials: Continuum thermomechanical theory and examples of control. Part I*, J. Mech. Phys. Solids 45 (1997), pp. 1203–1222.
- [29] V.I. Levitas, *Phase transitions in elastoplastic materials: Continuum thermomechanical theory and examples of control. Part II*, J. Mech. Phys. Solids 45 (1997), pp. 923–947.
- [30] H. Mao and P. Bell, *High pressure physics. Sustained static generation of 1.36 to 1.72 Mbar*, Science 200 (1978), pp. 1145–1147.
- [31] L. Vereshchagin and E. Zubova, *Measurement of the shearing stress of a number of substances at up to 100000 atm pressure*, Doklady Akademii Nauk SSSR 134 (1960), pp. 787–788.
- [32] V. Domnich, D. Ge, and Y. Gogotsi, *Indentation-induced phase transformations in semiconductors*, in *High Pressure Surface Science and Engineering*, Y. Gogotsi and V. Domnich, eds., Institute of Physics, Bristol, 2004, p. 381.